bioRxiv preprint doi: https://doi.org/10.1101/633347; this version posted May 9, 2019. The copyright holder for this preprint (which was not certified by peer review) is the author/funder, who has granted bioRxiv a license to display the preprint in perpetuity. It is made available under aCC-BY-NC-ND 4.0 International license.

# Quantifying nerve decussation abnormalities in the optic chiasm

Robert J. Puzniak [1], Khazar Ahmadi [1], Jörn Kaufmann [2], Andre Gouws [3], Antony B. Morland [3,4], Franco Pestilli *[5], Michael B. Hoffmann *†[1,6]

[1] Department of Ophthalmology, Otto-von-Guericke-University Magdeburg, Magdeburg, Germany

[2] Department of Neurology, Otto-von-Guericke-University Magdeburg, Magdeburg, Germany

[3] York Neuroimaging Centre, Department of Psychology, University of York, York, United Kingdom

[4] York Biomedical Research Institute, University of York, York, United Kingdom

[5] Department of Psychological and Brain Sciences, Indiana University, Bloomington, USA

[6] Center for Behavioral Brain Sciences, Magdeburg, Germany

* Shared senior authorships

† Corresponding author: Michael Hoffmann <michael.hoffmann@med.ovgu.de>; Department of Ophthalmology, Otto-von-Guericke-University Magdeburg, Leipziger Str. 44, 39120 Magdeburg, Germany

## Abstract

**Objective:** The human optic chiasm comprises partially crossing optic nerves. Here we used diffusion MRI (dMRI) for the in-vivo identification of optic chiasm abnormalities in albinism, i.e. enhanced optic nerves crossing.

**Methods:** In 9 individuals with albinism and 8 controls high-resolution 3T dMRI data were acquired and analysed with a set of methods for signal modelling [Diffusion Tensor (DT) and Constrained Spherical Deconvolution (CSD)], tractography, and statistical validation (LiFE, COMMIT, and SIFT). The number of crossing and non-crossing streamlines entered ROC-analyses to compare the discriminative power of the methods based on the area under curve (AUC). The dMRI results were cross-validated with fMRI estimates of misrouting in a subset of 6 albinotic individuals.

**Results:** We detected significant group differences in chiasmal crossing for both DT (p=0.018) and CSD (p=0.0003). ROC analyses indicated good performance of dMRI-based discrimination (AUC for

bioRxiv preprint doi: https://doi.org/10.1101/633347; this version posted May 9, 2019. The copyright holder for this preprint (which was not certified by peer review) is the author/funder, who has granted bioRxiv a license to display the preprint in perpetuity. It is made available under aCC-BY-NC-ND 4.0 International license.

DT and CSD: 0.81 and 0.96, respectively). Estimates of crossing strength obtained with dMRI and fMRI were correlated ($R^2$=0.65 and 0.83, respectively).

**Conclusions:** Especially CSD-based dMRI tractography provides an efficient approach to detect structural abnormalities in the optic chiasm.

**Significance:** Our findings demonstrate a novel anatomical approach for the individualized diagnostics of optic chiasm abnormalities.

## Highlights

- Diffusion MRI is capable of detecting structural abnormalities of the optic chiasm.
- Quantification of crossing strength in optic chiasm can be applied to albinism diagnostics.
- Optic chiasm is a powerful test model for neuroimaging methods resolving crossing fibers.

## Keywords

optic chiasm, albinism, diffusion MRI, functional MRI, crossing nerves

bioRxiv preprint doi: https://doi.org/10.1101/633347; this version posted May 9, 2019. The copyright holder for this preprint (which was not certified by peer review) is the author/funder, who has granted bioRxiv a license to display the preprint in perpetuity. It is made available under aCC-BY-NC-ND 4.0 International license.

# 1. Introduction

The optic chiasm is a core component of human visual system. Here the fate of the axons is decided, such that fibers from the nasal retina cross to the contralateral hemisphere, while those from the temporal retina do not cross and remain on the ipsilateral hemisphere. This partial decussation of the optic nerves guarantees that each hemisphere receives binocular input from the contralateral visual hemifield. Beyond its clinical relevance (Hoffmann & Dumoulin, 2015) and its relevance as a model for neuronal pathfinding in basic neuroscience (Petros, Rebsam, & Mason, 2008; Prieur & Rebsam, 2017) the optic chiasm poses a powerful model for the development of methods that allow the in-vivo-reconstruction of fiber tracts in the human brain. A common tool for this purpose is diffusion MRI (dMRI), which can be used to identify markers of the neuronal tissue organization (Basser, Mattiello, & LeBihan, 1994). This approach is confounded by tissues with a complex microstructure comprising a mixture of crossing and non-crossing nerves. These lead to misestimations of microstructural parameters (Oouchi et al., 2007) and the underlying fiber distribution (Jones, Knösche, & Turner, 2013). This is particularly relevant in areas with crossing fibers, which may affect as much as 90% of brain volume (Jeurissen, Leemans, Tournier, Jones, & Sijbers, 2013), making it an important challenge of dMRI.

The optic chiasm reflects the complex microstructure of other brain structures and has the decisive advantage that (i) the ratio of given crossing and non-crossing nerve fibers is a well-known ground truth and that (ii) human diseases are known, where this ratio is significantly altered. Based on the work of (Kupfer, Chumbley, & Downer, 1967), we have a clear understanding that in the neurotypical case 53% of nerve fibers in optic chiasm travel across the optic chiasm to contralateral lateral geniculate nucleus (LGN), while 47% project to the ipsilateral LGN. The optic chiasm was investigated in several studies evaluating

bioRxiv preprint doi: https://doi.org/10.1101/633347; this version posted May 9, 2019. The copyright holder for this preprint (which was not certified by peer review) is the author/funder, who has granted bioRxiv a license to display the preprint in perpetuity. It is made available under aCC-BY-NC-ND 4.0 International license.

accuracy of dMRI, such as the qualitative evaluation of tracking algorithms (Staempfli et al., 2007) or the quantification of fiber crossing strength in ex-vivo chiasms (Roebroeck et al., 2008). While both studies were successful in capturing qualitative features of the optic chiasm, neither provided an accurate quantitative estimation of crossing strength that was in agreement with expected values [Staempfli et al. (2007) performed qualitative analysis only, Roebroeck et al. (2008) estimates indicated that only up to 5% of nerve fibers cross to contralateral hemisphere]. The optic chiasm as a test-bed for differentiating crossing and non-crossing fibers can further be extended by the inclusion of known neuropathies affecting the human optic chiasm that reveal clear abnormalities. The most frequent of these rare conditions is albinism, which is associated with enhanced crossing of the optic nerve fibers (Guillery, 1986; Hagen, Houston, Hoffmann, Jeffery, & Morland, 2005; Morland, Hoffmann, Neveu, & Holder, 2002). Here the line of decussation that separates the ganglion cells with a crossed projection from those with an uncrossed projection and which is normally aligned with the fovea, is shifted by on average 8 degrees into the temporal retina (Hagen, Hoffmann, & Morland, 2008; Hagen, Houston, Hoffmann, & Morland, 2007; Hoffmann, Lorenz, Morland, & Schmidtborn, 2005). As a result, the crossing of the optic nerves is enhanced (Hoffmann & Dumoulin, 2015). Very recently, the first study to report group differences in chiasm tractography between albinism and controls using the Diffusion Tensor (DT) model was published (Ather et al., 2018). It demonstrated that dMRI can be used to identify, at the group level, differences in chiasmal connectivity between albinism and control groups.

The dMRI approach can be extended beyond the DT model (Basser et al., 1994), by incorporating an additional Constrained Spherical Deconvolution model [CSD; (Tournier, Calamante, & Connelly, 2007)], as well as the state-of-the-art tractography evaluation: Linear Fascicle Evaluation [LiFE; (Caiafa & Pestilli, 2017; F. Pestilli et al., 2014)], Convex

bioRxiv preprint doi: https://doi.org/10.1101/633347; this version posted May 9, 2019. The copyright holder for this preprint (which was not certified by peer review) is the author/funder, who has granted bioRxiv a license to display the preprint in perpetuity. It is made available under aCC-BY-NC-ND 4.0 International license.

Optimization Modeling for Microstructure Informed Tractography [COMMIT; (Daducci, Dal Palù, Lemkaddem, & Thiran, 2015; Daducci, Palu, Lemkaddem, & Thiran, 2013)], and Spherical-deconvolution Informed Filtering of Tractograms [SIFT; (R. E. Smith, Tournier, Calamante, & Connelly, 2013)]. In the present study, we compared the scope of these methods in identifying and quantifying an optic nerve fiber misrouting at the optic chiasm in albinism and its relation to fMRI-based estimates of misrouting extent. For CSD, we found a particularly strong correlation of the dMRI-based misrouting estimates with fMRI estimates. CSD thus opens the possibility to identify chiasmatic malformations at the individual level. Moreover, our investigations underscore the power of optic chiasm neuropathies as an efficient test-bed for tractography methods.

## 2. Methods

### 2.1 Participants

Nine participants with diagnosed albinism (5 females) and eight control subjects [6 females; no neurological or ophthalmological history; normal visual acuity (≥ 1.0, Freiburg Visual Acuity Test ((Bach, 1996)) and normal stereo vision (Donzis, Rappazzo, Burde, & Gordon, 1983; Lang & Lang, 1988)] were recruited for the study. Each participant was instructed about the purpose of the study and the methods involved and gave written informed study participation and data sharing consents. The study was approved by the Ethics Committee of the Otto-von-Guericke University Magdeburg, Magdeburg, Germany.

### 2.2 Data acquisition

All MRI data was acquired with a Siemens MAGNETOM Prisma 3 Tesla scanner with *syngo* MR D13D software and a 64-channel head coil. Diffusion and functional data was acquired

bioRxiv preprint doi: https://doi.org/10.1101/633347; this version posted May 9, 2019. The copyright holder for this preprint (which was not certified by peer review) is the author/funder, who has granted bioRxiv a license to display the preprint in perpetuity. It is made available under aCC-BY-NC-ND 4.0 International license.

during separate scanning sessions, during both sessions additional T1-weighted images were acquired.

### 2.2.1 T1-weighted data acquisition

T1-weighted images, obtained during both dMRI and fMRI scanning sessions, were collected in sagittal orientation using a 3D-MPRAGE sequence resolution [0.9 x 0.9 x 0.9 $mm^3$, FoV 230 x 230 mm, TR 2600ms, TE 4.46 ms, TI 1100 ms, flip angle 7°, image matrix: 256 × 256 x 176, acquisition time 11min:06s; (Mugler & Brookeman, 1990)].

### 2.2.2 dMRI data acquisition

The dMRI acquisition protocol was initiated with a localizer scan, followed by a T1-weighted MPRAGE scan and two diffusion-weighted scans [one with anterior-posterior (A>>P) and the other with posterior-anterior (P>>A) phase-encoding direction]. All data was collected during single continuous scanning session.

dMRI images were acquired with Echo-Planar Imaging (EPI) sequence [b-value 1600 s/$mm^2$, resolution 1.5 x 1.5 x 1.5 $mm^3$, anterior to posterior (A>>P) phase-encoding direction, FoV 220 x 220 mm, TR 9400 ms, TE 64.0 ms, acquisition time 22 min and 24 s]. Each scan was performed with 128 gradient directions, so the obtained diffusion-weighted data can be described as High Angular Resolution Diffusion Imaging [HARDI; (Tuch et al., 2002)] data. Gradient tables were generated using E. Caruyer's tool for q-space sampling (Caruyer, Lenglet, Sapiro, & Deriche, 2013). Diffusion-weighted volumes were evenly intersected by 10 non-diffusion weighted volumes for the purpose of motion correction. The second diffusion-weighted series was acquired with reversed phase-encoding direction relative to the previous scan, i.e., posterior to anterior (P>>A). Apart from that, all scan parameters were identical with those corresponding to previous acquisition. The acquisition of two diffusion-weighted series with opposite phase-encoding directions enhanced correction of

bioRxiv preprint doi: https://doi.org/10.1101/633347; this version posted May 9, 2019. The copyright holder for this preprint (which was not certified by peer review) is the author/funder, who has granted bioRxiv a license to display the preprint in perpetuity. It is made available under aCC-BY-NC-ND 4.0 International license.

geometrically induced distortions (Andersson, Skare, & Ashburner, 2003). Furthermore, the additional scans improved the signal-to-noise-ratio (SNR) of the total dMRI data.

### 2.2.3 fMRI data acquisition

Functional T2*-weighted images were acquired with EPI sequence [resolution 2.5 x 2.5 x 2.5 $mm^3$; 54 axial slices covering the whole brain, FoV 210 x 210 mm, TR 1500ms, TE 30.0 ms, flip angle 70°]. fMRI scanning session consisted of 6 functional scans, 168 time-frames (252s) each. The dominant eye of the albinotic participants was stimulated with moving bar apertures (9.5° in radius), as used in Ahmadi et al. (2018), covering either the left or the right visual hemifields (three repetitions per hemifield stimulation). All data was acquired during single continuous scanning session.

## 2.3 Data analysis

### 2.3.1 dMRI data analysis

#### 2.3.1.1 dMRI data preprocessing

The data was preprocessed using a combination of software toolboxes, MRtrix 3.0 (http://www.mrtrix.org/), FMRIB's FSL 5.0.9 (https://fsl.fmrib.ox.ac.uk/fsl/fslwiki), FreeSurfer 6.0.0 (https://surfer.nmr.mgh.harvard.edu/), ANTS 2.1.0 (http://stnava.github.io/ANTs/) and MrDiffusion (https://github.com/vistalab/vistasoft/tree/master/mrDiffusion). The preprocessing of the dMRI data from DICOM involved converting it to .mif format (compatible with MRtrix) using (mrconvert tool), denoising of the dMRI data [dwidenoise tool; (Veraart, Fieremans, & Novikov, 2016; Veraart, Novikov, et al., 2016)], removal of Gibbs ringing in the dMRI data [dwidegibbs command; (Kellner, Dhital, Kiselev, & Reisert, 2015)], estimation of susceptibility induced field in the dMRI data [topup tool; (Andersson et al., 2003)] using FSL (S. M. Smith et al., 2004), correction for geometry induced, eddy current and motion distortions in the

bioRxiv preprint doi: https://doi.org/10.1101/633347; this version posted May 9, 2019. The copyright holder for this preprint (which was not certified by peer review) is the author/funder, who has granted bioRxiv a license to display the preprint in perpetuity. It is made available under aCC-BY-NC-ND 4.0 International license.

dMRI data [eddy tool;(Andersson & Sotiropoulos, 2016)], and correction for the bias field in the dMRI data [ANTS, N4 algorithm; (Tustison et al., 2010)]. Finally, the dMRI data was coregistered to T1-weighted image aligned to Anterior Commissure - Posterior Commissure (AC-PC) space (mrAnatAverageAcpcNifti tool from MrDiffusion toolbox). The T1-weighted image was segmented into white, grey and subcortical grey matter and cerebrospinal fluid using FSL [FIRST command; (Patenaude, Smith, Kennedy, & Jenkinson, 2011)]. The obtained white matter masks were additionally manually corrected in the region of optic chiasm using T1-weighted image (**Figure 1A**, left and middle image).

#### 2.3.1.2 dMRI data modelling and tractography

Two distinct diffusion signal models were applied to the dMRI data - Diffusion Tensor [DT; (Basser et al., 1994)] and Constrained Spherical Deconvolution [CSD; (Descoteaux, Deriche, Le Bihan, Mangin, & Poupon, 2011; Tournier et al., 2007)]. The DT model was selected in order to compare the obtained results with previous studies which used this model only (Ather et al., 2018; Roebroeck et al., 2008). However, due to limited performance of DT model in case of populations of crossing fibers, an additional model, CSD, was also tested. The rationale behind this choice was to investigate whether the results can be improved when using a model that is more sensitive to crossing fibers populations, which at the same time benefits from the high angular resolution of collected dMRI data. Modelling for DT was performed with MRtrix tool tckgen (Tensor_Prob algorithm), where dMRI data in each voxel for each streamline was residually bootstrapped, priorly to DT fitting (Jones, 2008), so that tracking along principal eigenvectors of tensors was probabilistic. For the purpose of CSD modelling, an estimation of response from voxels containing only single fiber population (single fiber response, SFR) has been acquired using Tournier's approach [dwi2response tool with -tournier option (Tournier, Calamante, & Connelly, 2013)] for maximum harmonic order ($L_{max}$) equal to 6. The fibre orientation distribution functions

bioRxiv preprint doi: https://doi.org/10.1101/633347; this version posted May 9, 2019. The copyright holder for this preprint (which was not certified by peer review) is the author/funder, who has granted bioRxiv a license to display the preprint in perpetuity. It is made available under aCC-BY-NC-ND 4.0 International license.

[fODFs; (Jeurissen, Tournier, Dhollander, Connelly, & Sijbers, 2014)] have been obtained for 3 different maximum harmonic orders $L_{max}$ = 6, 8 and 10.

For the purpose of tracking for both DT and CSD, 4 regions of interest (ROIs) were manually drawn on T1 images for each individual data set - 2 covering intersections of left and right optic nerves and 2 covering intersections of left and right optic tracts. ROIs were placed so they were as close to optic chiasm as possible, but did not intersect it (**Figure 1A**, right image). Their width and height (in coronal view) had minimal values required to fully cover respective optic nerves or tracts, and each of ROIs was 3 voxels (4.5 mm) thick in order to ensure proper termination of streamlines during tractography. For each model, tracking was performed between 4 pairs of ROIs, where exactly one ROI was placed on optic nerve (left or right) and exactly one was placed on the optic tract (**Figure 1B**), so that the created streamlines groups could be either classified as crossing or non-crossing. For each pair of ROIs streamlines were generated twice, with switched definition of seed and target ROI, and merged into a single streamlines group, so that tracking results were not biased to the direction of tracking. Performed tracking was limited to previously obtained and manually corrected white matter masks [following Anatomically-Constrained Tractography framework; (R. E. Smith, Tournier, Calamante, & Connelly, 2012)]. Additionally, to reduce potential bias in tractography caused by the specific choice of tracking parameters, Ensemble Tractography (Takemura, Caiafa, Wandell, & Pestilli, 2016) was used for all the analyses. Accordingly, tractography was performed multiple times, with each run using a different set of parameters. The modified parameters were, specifically: fractional anisotropy threshold ($FA_{thresh}$) and maximum curvature angle between consecutive tracking steps ($Curv_{max}$). In case of CSD this list was extended by maximal harmonics order ($L_{max}$) of the fitted fODFs. Notably, the CSD used SFR obtained for only single $L_{max}$=6. The exact values of used parameters are displayed in the **Table 1.**

bioRxiv preprint doi: https://doi.org/10.1101/633347; this version posted May 9, 2019. The copyright holder for this preprint (which was not certified by peer review) is the author/funder, who has granted bioRxiv a license to display the preprint in perpetuity. It is made available under aCC-BY-NC-ND 4.0 International license.

| | DT | CSD |
|---|---|---|
| **$FA_{thresh}$** | 0.04, 0.08 | 0.04, 0.08 |
| **$Curv_{max}$ [°]** | 30, 45, 60 | 30, 45, 60 |
| **SFRs $L_{max}$** | - | 6 |
| **fODFs $L_{max}$** | - | 6,8,10 |

**Table 1. Tractography parameters.** Sets of parameters used in generating DT- (left column) and CSD-based (right column) tractograms. Rows correspond to different parameters, from top to bottom, respectively, the cut-off FA threshold ($FA_{thresh}$), maximum angle between consecutive tracking steps ($Curv_{max}$), maximal harmonic order of SFR (SFR $L_{max}$) and fODF (fODFs $L_{max}$).

For each subject, for a given combination of parameters tractography was performed for 4 distinct seed-target ROI pairs, and for each pair of ROIs it was performed twice (reversal of seed-target definitions), with 139 000 seeds (random locations within seed ROI, which serve as starting points for tracking) and 1000 tracking attempts per seed. This resulted in a total of $6.672*10^9$ tracking attempts per subject when using DT model and $20.016*10^9$ attempts for CSD-based analysis. The DT-based tracking used Tensor_Prob algorithm (Jones, 2008), the CSD-based was performed with iFOD2 algorithm (Tournier, Calamante, & Connelly, 2010). Due to the requirements of the subsequent validation of tractograms, an additional whole brain tractogram was generated. It shared most of the features of the CSD-based ROI to ROI tractography, save for the whole brain seeding mechanism [dynamic seeding; (R. E. Smith, Tournier, Calamante, & Connelly, 2015)] and a fixed number of generated streamlines per combination of parameters ($1.5*10^6$, for a combined total of $27*10^9$ streamlines).

bioRxiv preprint doi: https://doi.org/10.1101/633347; this version posted May 9, 2019. The copyright holder for this preprint (which was not certified by peer review) is the author/funder, who has granted bioRxiv a license to display the preprint in perpetuity. It is made available under aCC-BY-NC-ND 4.0 International license.

#### 2.3.1.3 Tractography validation

The tractography results were used in subsequent statistical analyses (Franco Pestilli, 2015; Takemura et al., 2016)). In addition, in order to further investigate the robustness of the results on intra-study level, the obtained tractograms were additionally validated with 3 separate algorithms: (1) Linear Fascicle Evaluation [LiFE; (Caiafa & Pestilli, 2017; F. Pestilli et al., 2014; Takemura et al., 2016)],(2) The Convex Optimization Modelling for Microstructure Informed Tractography [COMMIT; (Daducci et al., 2015, 2013)], and (3) the Spherical-deconvolution Informed Filtering of Tractograms [SIFT; (R. E. Smith et al., 2013)]:

**(1) LiFE** (Caiafa & Pestilli, 2017; F. Pestilli et al., 2014; Takemura et al., 2016)**.** LiFE evaluates individual streamline paths by scoring their contribution to predicting the measured diffusion signal across brain white matter voxels; good streamlines positively contribute to predicting the dMRI signal, poor streamline paths do not contribute positively to predicting the measured dMRI signal.

**(2) COMMIT** (Daducci et al., 2015, 2013)**.** The COMMIT framework follows a similar rationale to LiFE, extending the range of model parameters that can be used to predicting the dMRI signal (i.e., it adds additional parameters to model both intra- and extra-axonal cellular contributions to the dMRI signal prediction). More specifically, we used the Stick-Zeppelin-Ball model as in (Panagiotaki et al., 2012), where one intra-axonal and two extra-axonal compartments contributed to modelling and predicting the dMRI signal.

**(3) SIFT** (R. E. Smith et al., 2013). SIFT filters a tractography solution by eliminating the streamlines so to optimize a model that matches the densities generated from the streamline counts with the size of the modelled fiber Orientation Distribution Functions (fODFs) estimated from the signal within individual voxels (R. E. Smith et al., 2015).

bioRxiv preprint doi: https://doi.org/10.1101/633347; this version posted May 9, 2019. The copyright holder for this preprint (which was not certified by peer review) is the author/funder, who has granted bioRxiv a license to display the preprint in perpetuity. It is made available under aCC-BY-NC-ND 4.0 International license.

The methods used for validation had different requirements. LiFE and COMMIT can operate on a subset of the brain voxels and tractography. For these two methods, validation was performed on the set of streamlines tracked between pairs of ROIs placed in the anterior and posterior portions of the optic chiasm. The resulting groups of validated streamlines were subsequently sorted into streamlines projecting at the optic chiasm ipsi- and contralaterally. SIFT instead performs a global validation, which requires a whole brain tractogram as an input. In this case, a different whole brain tractogram was generated and then validated using SIFT. Validated streamlines were subsequently divided into groups (crossing the optic chiasm ipsi- and contra-laterally) using the same set of ROIs as used for the analysis with LiFE and COMMIT. The SIFT validation was applied to the CSD-based tractograms only, as using it together with DT model is neither an advised analysis strategy, nor allows for direct comparison of results with previous studies using DT.

#### 2.3.1.4 Quantitative and statistical analysis

For every participant the total number of non-crossing and crossing streamlines was obtained by summing number of respective streamlines. In order to reduce the dimensionality of the results and to allow for cross-study comparison  the decussation index [$I_D$; as defined in Ather et al. (2018)] was applied::

$$I_D = \frac{streamlines_{crossing}}{streamlines_{crossing} + streamlines_{non-crossing}}$$

where $streamlines_{crossing}$ and $streamlines_{non\text{-}crossing}$ correspond to total number of crossing and non-crossing streamlines, respectively, and which was calculated for each participant separately.

The estimates of crossing, expressed either by the pair of numbers corresponding to crossing and non-crossing streamlines or a single value $I_D$, were used for a Receiver Operating Characteristic (ROC) curve analysis, where they entered as predictor variables. The classification was performed with a logistic regression for binomial distributions (as the

bioRxiv preprint doi: https://doi.org/10.1101/633347; this version posted May 9, 2019. The copyright holder for this preprint (which was not certified by peer review) is the author/funder, who has granted bioRxiv a license to display the preprint in perpetuity. It is made available under aCC-BY-NC-ND 4.0 International license.

analysis was focused on two groups) using the logit link function. The obtained probability estimates obtained from the logistic regression were subsequently used for the computation of ROC curves and calculation of corresponding AUCs which were used as an estimation of accuracy of detection of chiasmatic abnormalities for different models and validation methods (or lack thereof).

### 2.3.2 fMRI data analysis

#### 2.3.2.1 fMRI data preprocessing

fMRI data were preprocessed using FreeSurfer 6.0.0, FMRIB's FSL 5.0.9, Vistasoft and a toolbox developed by Kendrick Kay (https://github.com/kendrickkay/alignvolumedata). The T1-weighted image was automatically segmented into white matter volume and cortical surface using FreeSurfer. fMRI data was corrected for motion with FSL, averaged for each participant and subsequently aligned to the T1-weighted image with Vistasoft and Kendrick Kay's alignment toolbox. The cortical surface reconstruction at the white and grey matter boundary, as well as rendering of smoothed 3D mesh (Wandell, Chial, & Backus, 2000) was performed with Vistasoft.

#### 2.3.2.2 Population receptive field (pRF) mapping

The estimation of pRF properties, delineation of the visual areas and visualization on the smoothed mesh surface were performed using Vistasoft, as described in a previous study (Ahmadi et al., 2018). Polar angle and eccentricity maps were extracted and the misrouting extent was measured by calculating the eccentricity [in degrees of visual angle] for the abnormal representation in a ROI drawn at the fundus of calcarine sulcus that coincided with the representation of the horizontal meridian.

bioRxiv preprint doi: https://doi.org/10.1101/633347; this version posted May 9, 2019. The copyright holder for this preprint (which was not certified by peer review) is the author/funder, who has granted bioRxiv a license to display the preprint in perpetuity. It is made available under aCC-BY-NC-ND 4.0 International license.

## 3. Results

In order to compare different dMRI-based approaches to assess optic chiasm integrity, we assessed (i) non-validated DT-based tractograms, (ii) non-validated CSD-based tractograms, and (iii) the impact of track validation on the identification of chiasmal abnormalities at the both group and individual level.

*(i) Scope of non-validated DT-based tractograms for detection of chiasma abnormalities.*

In analogy to Ather et al. (Ather et al., 2018) we quantified the crossing strength by comparing the streamline counts for crossing and non-crossing streamlines as depicted in **Figure 1B** and **C**. In order to compare different dMRI-based approaches to assess optic chiasm integrity, we further expressed the extent of crossing at the optic chiasm in the albinotic and the control group via $I_D$ (**Figure 1D**) as detailed in Methods. In accordance with Ather et al. (2018), our results demonstrated a significant $I_D$ difference between the albinism and control group [median (mean±MSE) decussation index: 17.87% (40.48%±40.09) and 6.34% (5.75%±4.42), respectively; p=0.018]. A ROC analysis to assess the accuracy of the detection of chiasmatic abnormalities at an individual level, yielded an AUC of 0.81, i.e. similar to that reported by Ather et al. (AUC=0.73). As a consequence, while the detection of abnormalities is feasible at the group level, it has only around 80% accuracy at the individual level.

*(ii) Comparison of non-validated CSD- and DT-based tractograms.*

The CSD-based approach also allowed for the detection of differences in the chiasm crossing at the group level [median (mean±MSE) decussation index 43.53% (41.06%±15.21) and 18.48% (19.08%±6.34), for albinism and controls respectively; p=0.0003)] as depicted in (**Figure 1 F** and **G**). Importantly, the ROC analysis yielded a higher AUC, i.e. 0.96, than the DT-based approach, which underlines a greater discriminative power at the individual level for CSD derived streamlines. Interestingly, $I_D$s vary across the albinotic subjects, for both the

bioRxiv preprint doi: https://doi.org/10.1101/633347; this version posted May 9, 2019. The copyright holder for this preprint (which was not certified by peer review) is the author/funder, who has granted bioRxiv a license to display the preprint in perpetuity. It is made available under aCC-BY-NC-ND 4.0 International license.

CSD and especially the DT model. We now tested whether this variability in $I_D$ across albinotic subjects is related to the well-known variability of the extent of misrouting in albinism, which is particularly evident in cortical measures of the representation abnormality in albinism (Hoffmann et al., 2005; Hoffmann, Tolhurst, Moore, & Morland, 2003). For this purpose, we correlated the dMRI-derived $I_D$ of six albinotic participants with the strength of their misrouting as determined from fMRI-based pRF mapping [see Methods]. There was a clearly significant positive correlation for the CSD model ($R^2$ =0.83; p=0.012; **Figure 1H**), while there was only a non-significant trend of a positive correlation for the DT model ($R^2$=0.65, p=0.052; **Figure 1E**). This indicates an unexpected precision in the dMRI-based detection of misrouting in albinism, actually reflecting the extent of misrouting.

*(iii) Relevance of tractography validation.*

With the previous analyses being exclusively performed for non-validated tractograms, we now assessed the effect of tractography validation as detailed in Methods for the DT and CSD modelling approaches. In analogy to the above analyses, their outcome is quantified via the ROC-derived AUC values and $R^2$ values for the correlation of ID and fMRI-based extent of misrouting (**Table 2 and Figures A.1, B.1** and **B.2**). No systematic increase of ROC and AUC values was observed, only a 6%-increase of AUC for the COMMIT validation of the DT model. Finally, it should be noted that, similar to previous reports on streamline counts at the optic chiasm, as in Roebroeck et al. (2008) and Ather et al. (2018), the crossing ratio is below 50% for all controls and most albinotic participants (**Figure 1C** and **F**; **Figure A.1**).

bioRxiv preprint doi: https://doi.org/10.1101/633347; this version posted May 9, 2019. The copyright holder for this preprint (which was not certified by peer review) is the author/funder, who has granted bioRxiv a license to display the preprint in perpetuity. It is made available under aCC-BY-NC-ND 4.0 International license.

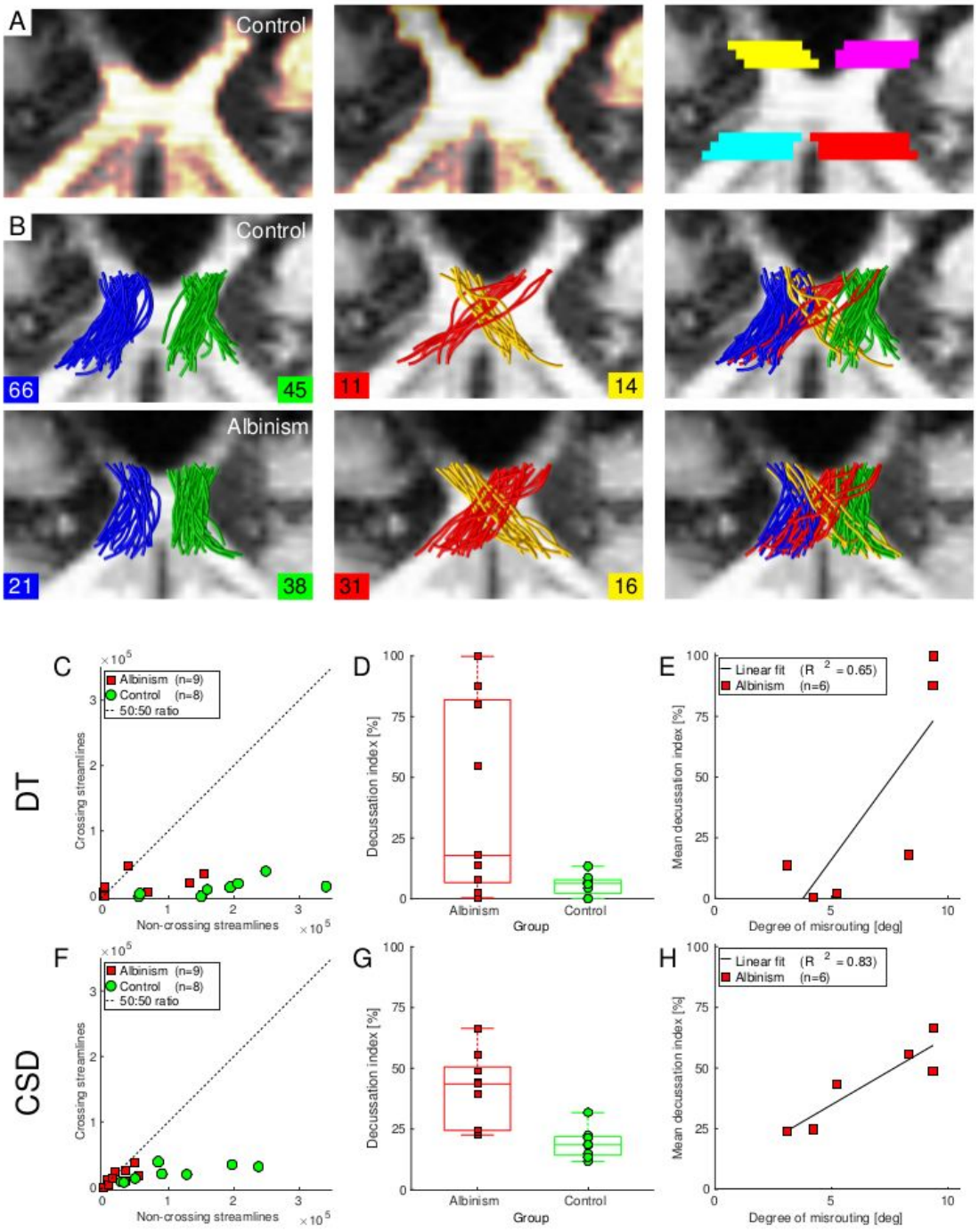


**Figure 1. White matter mask, ROIs definition, example of tractography and quantitative results. A.** T1-weighted image of exemplary control subject overlaid with automatically generated white matter mask (left column), manually corrected mask (middle column) and ROIs covering intersections of ends of optic nerves and beginnings of optic tracts (right column). **B.** Exemplary subsets of tractograms (0.125% of a total number of streamlines) for control (top row) and albinism (bottom row) participants, i.e., streamlines projecting through the chiasm ipsilaterally (non-crossing; left column), contralaterally (crossing; middle column), and a combination of both streamlines (right column). **C.** Numbers of crossing and non-crossing streamlines calculated from

bioRxiv preprint doi: https://doi.org/10.1101/633347; this version posted May 9, 2019. The copyright holder for this preprint (which was not certified by peer review) is the author/funder, who has granted bioRxiv a license to display the preprint in perpetuity. It is made available under aCC-BY-NC-ND 4.0 International license.

tractograms based on DT model. **D.** Numbers of crossing vs. non-crossing streamlines calculated from tractograms based on DT model expressed with $I_D$. **E.** Correlation between estimates of the extent of crossing obtained with dMRI using DT model and fMRI-based pRF mapping. **F.** Numbers of crossing streamlines plotted vs non-crossing streamlines calculated from tractograms based on CSD model. **G.** Numbers of crossing and non-crossing streamlines calculated from tractograms based on CSD model expressed with $I_D$. **H.** Correlation between estimates of crossing obtained with dMRI using CSD model and fMRI-based pRF mapping.

| | **AUC** | | **$R^2$** | |
|---|---|---|---|---|
| | *DT* | *CSD* | *DT* | *CSD* |
| **Non-validated** | 0.81 | 0.96 | 0.65 | 0.83 |
| **LiFE** | 0.74 | 0.83 | 0.36 | 0.38 |
| **COMMIT** | 0.86 | 0.92 | 0.50 | 0.52 |
| **SIFT** | - | 0.96 | - | 0.54 |

**Table 2. Accuracy of group classification based on dMRI results and their correlation with fMRI results.** AUC values obtained from ROC analysis for DT and CSD models (left column) and $R^2$ values obtained from linear regression of dMRI and fMRI estimates of crossing strength for DT and CSD models (right column). Rows correspond to different validation methods employed (see **subsection 2.3.1.3**).

## 4. Discussion

We reported a significant difference of the decussation index ($I_D$) between the albinism and control group, which was more pronounced for the CSD than for the DT model. The ROC analyses for the CSD model suggests its strong potential as an aid for individualized diagnostics. This is further supported by the linear correlation of the CSD-derived $I_D$ values with the extent of misrouting estimated from fMRI. Further analyses for the tested models and tractography validation methods consistently confirmed that the CSD model yields better classification accuracy for all investigated approaches. The tractography validation methods did not consistently improve classification performance.

bioRxiv preprint doi: https://doi.org/10.1101/633347; this version posted May 9, 2019. The copyright holder for this preprint (which was not certified by peer review) is the author/funder, who has granted bioRxiv a license to display the preprint in perpetuity. It is made available under aCC-BY-NC-ND 4.0 International license.

Our results are in accordance with those reported by Ather et al. (2018) demonstrating that dMRI can detect structural abnormalities of the optic chiasm at a group level. Notably, the findings were reproduced despite several differences in the study design, such as acquisition protocols, preprocessing pipeline, implementation of DT model, tracking algorithm and sample size, which indicates the robustness of the effect. The obtained numerical values of mean $I_D$ do differ though. While Ather et al. (2018) report mean $I_D$ for albinism and controls of 42.0% ± 18.7 and 27.8% ± 17.5, respectively, we note that while our estimates of crossing in albinism show similar value (40.48% ± 40.09), we underestimate crossing in the control group (5.75% ± 4.42). Our values for controls, however, do very well correspond with those reported by Roebroeck et al. (Roebroeck et al., 2008). In their study, ultra-high field (9.4T) and sub-millimetre resolution (156 x 156 x 312 μm) dMRI analysis of 3 ex-vivo human chiasms (analysis also using the DT model), they also reported values corresponding to $I_D \approx$ 5%.

It is important to note, that all the estimates of $I_D$ inferred from DT based dMRI analysis which were reported thus far [Roebroeck et. al (2008), Ather et. al. (2018)] heavily underestimate the actual ground truth ratio of crossing to non-crossing nerves in optic chiasm (53:47, respectively) as reported by Kupfer et al.(1967). One of the causes of this is an intrinsic limitation of the DT model, as it assumes only one, dominant direction per voxel and as such is ill-defined for populations of crossing fibers. Consequently, the application of DT in those cases leads to neglect of valid fibers and erroneous estimates of primal direction (Wiegell, Larsson, & Wedeen, 2000). Taking into account the given limitation of DT and nature of chiasm anatomy, we extended our study by incorporating a CSD model. This model is believed to be superior to DT when resolving crossing fibers and additionally benefits from the HARDI acquisition protocol we used for our data. Accordingly, we found that for non-validated tractograms based on the CSD model the mean $I_D$ values for albinism and control (41.06 ± 15.21 and 19.08 ± 6.34 %, respectively) are higher and closer to biological

bioRxiv preprint doi: https://doi.org/10.1101/633347; this version posted May 9, 2019. The copyright holder for this preprint (which was not certified by peer review) is the author/funder, who has granted bioRxiv a license to display the preprint in perpetuity. It is made available under aCC-BY-NC-ND 4.0 International license.

ground truth than those we report for DT. The improvement in results introduced by the CSD model is also reflected in the cross-modality validation with fMRI ($R^2$ value for linear function fit = 0.83, compared to 0.65 for DT) and calculated AUC (0.96 compared to 0.81). Those findings are well in agreement with theoretical expectations and provide a strong argument for using models more fitting crossing fibers population in future studies on chiasmal connectivity. Counter-intuitively, the application of tractography validation methods did not improve results. While it should be noted that results for non- and validated tractograms in both models were consistent (**Figure A.1**) and the demonstrated pattern was preserved, the $I_D$ derived from validated tractograms did not consistently improve calculated, nor did it show a closer correlation with the fMRI-based estimates of the extent of misrouting

## 4.2 Limitations

The study was mainly limited by the challenge of imaging of optic chiasm. Specifically, the small size of the optic chiasm and its location in highly heterogeneous brain region impact the quality of dMRI images and subsequent analysis stages, such as tractography. The design of our acquisition protocol and preprocessing pipeline allowed us to address those challenges, we, however, note that this study aspect may be in future further improved with emerging methods (Bastiani et al., 2019).

## 4.3 Practical relevance

A key objective of our study was to explore the scope of dMRI-based assessment of chiasm integrity and hence its potential as a diagnostic. This is particularly relevant as the identification of chiasmatic abnormalities is a key for the correct diagnosis, e.g. in forms of albinism with also mild pigmentation deficits (Montoliu et al., 2014). Functional tests established for this purpose (Apkarian, Reits, Spekreijse, & Van Dorp, 1983; Hagen et al., 2008) have the disadvantage that they require to activate the visual system and rely on the

bioRxiv preprint doi: https://doi.org/10.1101/633347; this version posted May 9, 2019. The copyright holder for this preprint (which was not certified by peer review) is the author/funder, who has granted bioRxiv a license to display the preprint in perpetuity. It is made available under aCC-BY-NC-ND 4.0 International license.

cooperation of the often severely visually impaired participants. While procedures based on purely anatomical MRI procedures do not allow an individualised identification (Schmitz et al., 2003), our results indicate that dMRI combined with CSD modelling might be able to fill this gap. In fact, testing a greater sample of participants is now required.

## 5. Conclusions

We investigated the application of state-of-the-art dMRI to detect optic chiasm abnormalities and report CSD-based models to identify abnormalities with high accuracy (AUC=0.96) and to correlate well with functional (fMRI) measures of the optic nerve misrouting ($R^2$=0.83) dMRI combined with CSD-modelling therefore appears to be of promise for the development of an individualized identification of chiasmatic abnormalities. Moreover, our investigations highlight the great value of the optic chiasm as a test-bed for dMRI methods-optimization. In order to further support these activities, we are in the process of making the data set publicly available for the benefit of the general neuroimaging community.

**Acknowledgements**

The authors thank the study participants. This work was supported by European Union's Horizon 2020 research and innovation programme under the Marie Sklodowska-Curie grant agreement (No. 641805) and by the German research foundation (DFG, HO 2002 10-3) to M.B.H. Additional support was provided by NSF IIS-1636893, NSF BCS-1734853, NIH UL1TR002529, a Microsoft Research Award, a Google Cloud Award, the Indiana University Areas of Emergent Research initiative "Learning: Brains, Machines, Children" and Pervasive Technology Institute to F.P.

bioRxiv preprint doi: https://doi.org/10.1101/633347; this version posted May 9, 2019. The copyright holder for this preprint (which was not certified by peer review) is the author/funder, who has granted bioRxiv a license to display the preprint in perpetuity. It is made available under aCC-BY-NC-ND 4.0 International license.

# 6. Legends

**Table 1. Tractography parameters.** Sets of parameters used in generating DT- (left column) and CSD-based (right column) tractograms. Rows correspond to different parameters, from top to bottom, respectively, the cut-off FA threshold ($FA_{thresh}$), maximum angle between consecutive tracking steps ($Curv_{max}$), maximal harmonic order of SFR (SFR $L_{max}$) and fODF (fODFs $L_{max}$).

**Figure 1. White matter mask, ROIs definition, example of tractography and quantitative results. A.** T1-weighted image of exemplary control subject overlaid with automatically generated white matter mask (left column), manually corrected mask (middle column) and ROIs covering intersections of ends of optic nerves and beginnings of optic tracts (right column). **B.** Exemplary subsets of tractograms (0.125% of a total number of streamlines) for control (top row) and albinism (bottom row) participants, i.e., streamlines projecting through the chiasm ipsilaterally (non-crossing; left column), contralaterally (crossing; middle column), and a combination of both streamlines (right column). **C.** Numbers of crossing and non-crossing streamlines calculated from tractograms based on DT model. **D.** Numbers of crossing vs. non-crossing streamlines calculated from tractograms based on DT model expressed with $I_D$. **E.** Correlation between estimates of the extent of crossing obtained with dMRI using DT model and fMRI-based pRF mapping. **F.** Numbers of crossing streamlines plotted vs non-crossing streamlines calculated from tractograms based on CSD model. **G.** Numbers of crossing and non-crossing streamlines calculated from tractograms based on CSD model expressed with $I_D$. **H.** Correlation between estimates of crossing obtained with dMRI using CSD model and fMRI-based pRF mapping.

**Table 2. Accuracy of group classification based on dMRI results and their correlation with fMRI results.** AUC values obtained from ROC analysis for DT and CSD models (left column) and $R^2$ values obtained from linear regression of dMRI and fMRI estimates of crossing strength for DT and CSD models (right column). Rows correspond to different validation methods employed (see **subsection 2.3.1.3**).

**Figure A.1. Streamline counts for all tested combinations of diffusion models and validation methods.** Numbers of crossing (x-axis) and non-crossing (y-axis) streamlines calculated from tractograms based on DT (left column) and CSD (right column) models. Rows correspond to different tested validation methods, from the

bioRxiv preprint doi: https://doi.org/10.1101/633347; this version posted May 9, 2019. The copyright holder for this preprint (which was not certified by peer review) is the author/funder, who has granted bioRxiv a license to display the preprint in perpetuity. It is made available under aCC-BY-NC-ND 4.0 International license.

top to bottom, respectively: absence of validation, validation with LiFE, validation with COMMIT framework employing multicompartment SZB model and validation with SIFT.

**Figure B.1. Qualitative tracking results for exemplary control subject.** Exemplary subsets of tractograms (1% of a total number of streamlines) for DT- (left column) and CSD-based (right column) based modelling. Tracks traversing optic chiasm ipsilaterally (left sub-columns) and tracks crossing optic chiasm to contralateral brain hemisphere (middle sub-columns) were merged into single group of tracks (right sub-columns). Rows correspond to different tested validation methods, from the top to bottom, respectively: absence of validation, validation with LiFE, validation with COMMIT framework employing multicompartment SZB model and validation with SIFT.

**Figure B.2. Qualitative tracking results for exemplary participant with albinism.** Conventions as in **Figure B.1**.

bioRxiv preprint doi: https://doi.org/10.1101/633347; this version posted May 9, 2019. The copyright holder for this preprint (which was not certified by peer review) is the author/funder, who has granted bioRxiv a license to display the preprint in perpetuity. It is made available under aCC-BY-NC-ND 4.0 International license.

## 7. References

Ahmadi, K., Fracasso, A., van Dijk, J. A., Kruijt, C., van Genderen, M., Dumoulin, S. O., & Hoffmann, M. B. (2018). Altered organization of the visual cortex in FHONDA syndrome. *NeuroImage*. https://doi.org/10.1016/j.neuroimage.2018.02.053

Andersson, J. L. R., Skare, S., & Ashburner, J. (2003). How to correct susceptibility distortions in spin-echo echo-planar images: application to diffusion tensor imaging. *NeuroImage*, *20*(2), 870–888.

Andersson, J. L. R., & Sotiropoulos, S. N. (2016). An integrated approach to correction for off-resonance effects and subject movement in diffusion MR imaging. *NeuroImage*, *125*, 1063–1078.

Apkarian, P., Reits, D., Spekreijse, H., & Van Dorp, D. (1983). A decisive electrophysiological test for human albinism. *Electroencephalography and Clinical Neurophysiology*, *55*(5), 513–531.

Ather, S., Proudlock, F. A., Welton, T., Morgan, P. S., Sheth, V., Gottlob, I., & Dineen, R. A. (2018). Aberrant visual pathway development in albinism: From retina to cortex. *Human Brain Mapping*. https://doi.org/10.1002/hbm.24411

Bach, M. (1996). The Freiburg Visual Acuity Test - Automatic Measurement of Visual Acuity. *Optometry and Vision Science: Official Publication of the American Academy of Optometry*, *73*(1), 49–53.

Basser, P. J., Mattiello, J., & LeBihan, D. (1994). MR diffusion tensor spectroscopy and imaging. *Biophysical Journal*, *66*(1), 259–267.

Bastiani, M., Andersson, J. L. R., Cordero-Grande, L., Murgasova, M., Hutter, J., Price, A. N., … Sotiropoulos, S. N. (2019). Automated processing pipeline for neonatal diffusion MRI in the developing Human Connectome Project. *NeuroImage*, *185*, 750–763.

Caiafa, C. F., & Pestilli, F. (2017). Multidimensional encoding of brain connectomes.

bioRxiv preprint doi: https://doi.org/10.1101/633347; this version posted May 9, 2019. The copyright holder for this preprint (which was not certified by peer review) is the author/funder, who has granted bioRxiv a license to display the preprint in perpetuity. It is made available under aCC-BY-NC-ND 4.0 International license.

https://doi.org/10.1101/107607

Caruyer, E., Lenglet, C., Sapiro, G., & Deriche, R. (2013). Design of multishell sampling schemes with uniform coverage in diffusion MRI. *Magnetic Resonance in Medicine: Official Journal of the Society of Magnetic Resonance in Medicine / Society of Magnetic Resonance in Medicine*, *69*(6), 1534–1540.

Daducci, A., Dal Palù, A., Lemkaddem, A., & Thiran, J.-P. (2015). COMMIT: Convex optimization modeling for microstructure informed tractography. *IEEE Transactions on Medical Imaging*, *34*(1), 246–257.

Daducci, A., Palu, A. D., Lemkaddem, A., & Thiran, J.-P. (2013). A convex optimization framework for global tractography. In *2013 IEEE 10th International Symposium on Biomedical Imaging*. https://doi.org/10.1109/isbi.2013.6556527

Descoteaux, M., Deriche, R., Le Bihan, D., Mangin, J.-F., & Poupon, C. (2011). Multiple q-shell diffusion propagator imaging. *Medical Image Analysis*, *15*(4), 603–621.

Donzis, P. B., Rappazzo, J. A., Burde, R. M., & Gordon, M. (1983). Effect of Binocular Variations of Snellen's Visual Acuity on Titmus Stereoacuity. *Archives of Ophthalmology*, *101*(6), 930–932.

Guillery, R. W. (1986). Neural abnormalities of albinos. *Trends in Neurosciences*. https://doi.org/10.1016/0166-2236(86)90115-3

Hagen, E. A. H., Houston, G. C., Hoffmann, M. B., Jeffery, G., & Morland, A. B. (2005). Retinal abnormalities in human albinism translate into a reduction of grey matter in the occipital cortex. *European Journal of Neuroscience*. https://doi.org/10.1111/j.1460-9568.2005.04433.x

Hagen, E. A. H. von D., Hoffmann, M. B., & Morland, A. B. (2008). Identifying Human Albinism: A Comparison of VEP and fMRI. *Investigative Opthalmology & Visual Science*. https://doi.org/10.1167/iovs.07-0458

Hagen, E. A. H. von D., Houston, G. C., Hoffmann, M. B., & Morland, A. B. (2007).

bioRxiv preprint doi: https://doi.org/10.1101/633347; this version posted May 9, 2019. The copyright holder for this preprint (which was not certified by peer review) is the author/funder, who has granted bioRxiv a license to display the preprint in perpetuity. It is made available under aCC-BY-NC-ND 4.0 International license.

Pigmentation predicts the shift in the line of decussation in humans with albinism. *European Journal of Neuroscience*. https://doi.org/10.1111/j.1460-9568.2007.05303.x

Hoffmann, M. B., & Dumoulin, S. O. (2015). Congenital visual pathway abnormalities: a window onto cortical stability and plasticity. *Trends in Neurosciences*, *38*(1), 55–65.

Hoffmann, M. B., Lorenz, B., Morland, A. B., & Schmidtborn, L. C. (2005). Misrouting of the optic nerves in albinism: estimation of the extent with visual evoked potentials. *Investigative Ophthalmology & Visual Science*, *46*(10), 3892–3898.

Hoffmann, M. B., Tolhurst, D. J., Moore, A. T., & Morland, A. B. (2003). Organization of the visual cortex in human albinism. *The Journal of Neuroscience: The Official Journal of the Society for Neuroscience*, *23*(26), 8921–8930.

Jeurissen, B., Leemans, A., Tournier, J.-D., Jones, D. K., & Sijbers, J. (2013). Investigating the prevalence of complex fiber configurations in white matter tissue with diffusion magnetic resonance imaging. *Human Brain Mapping*, *34*(11), 2747–2766.

Jeurissen, B., Tournier, J.-D., Dhollander, T., Connelly, A., & Sijbers, J. (2014). Multi-tissue constrained spherical deconvolution for improved analysis of multi-shell diffusion MRI data. *NeuroImage*, *103*, 411–426.

Jones, D. K. (2008). Tractography gone wild: probabilistic fibre tracking using the wild bootstrap with diffusion tensor MRI. *IEEE Transactions on Medical Imaging*, *27*(9), 1268–1274.

Jones, D. K., Knösche, T. R., & Turner, R. (2013). White matter integrity, fiber count, and other fallacies: the do’s and don'ts of diffusion MRI. *NeuroImage*, *73*, 239–254.

Kellner, E., Dhital, B., Kiselev, V. G., & Reisert, M. (2015). Gibbs-ringing artifact removal based on local subvoxel-shifts. *Magnetic Resonance in Medicine: Official Journal of the Society of Magnetic Resonance in Medicine / Society of Magnetic Resonance in Medicine*, *76*(5), 1574–1581.

Kupfer, C., Chumbley, L., & Downer, J. C. (1967). Quantitative histology of optic nerve, optic

bioRxiv preprint doi: https://doi.org/10.1101/633347; this version posted May 9, 2019. The copyright holder for this preprint (which was not certified by peer review) is the author/funder, who has granted bioRxiv a license to display the preprint in perpetuity. It is made available under aCC-BY-NC-ND 4.0 International license.

tract and lateral geniculate nucleus of man. *Journal of Anatomy*, *101*(Pt 3), 393–401.

Lang, J. I., & Lang, T. J. (1988). Eye Screening with the Lang Stereotest. *The American Orthoptic Journal*, *38*(1), 48–50.

Montoliu, L., Grønskov, K., Wei, A.-H., Martínez-García, M., Fernández, A., Arveiler, B., … Li, W. (2014). Increasing the complexity: new genes and new types of albinism. *Pigment Cell & Melanoma Research*, *27*(1), 11–18.

Morland, A. B., Hoffmann, M. B., Neveu, M., & Holder, G. E. (2002). Abnormal visual projection in a human albino studied with functional magnetic resonance imaging and visual evoked potentials. *Journal of Neurology, Neurosurgery, and Psychiatry*, *72*(4), 523–526.

Mugler, J. P., 3rd, & Brookeman, J. R. (1990). Three-dimensional magnetization-prepared rapid gradient-echo imaging (3D MP RAGE). *Magnetic Resonance in Medicine: Official Journal of the Society of Magnetic Resonance in Medicine / Society of Magnetic Resonance in Medicine*, *15*(1), 152–157.

Oouchi, H., Yamada, K., Sakai, K., Kizu, O., Kubota, T., Ito, H., & Nishimura, T. (2007). Diffusion anisotropy measurement of brain white matter is affected by voxel size: underestimation occurs in areas with crossing fibers. *AJNR. American Journal of Neuroradiology*, *28*(6), 1102–1106.

Panagiotaki, E., Schneider, T., Siow, B., Hall, M. G., Lythgoe, M. F., & Alexander, D. C. (2012). Compartment models of the diffusion MR signal in brain white matter: a taxonomy and comparison. *NeuroImage*, *59*(3), 2241–2254.

Patenaude, B., Smith, S. M., Kennedy, D. N., & Jenkinson, M. (2011). A Bayesian model of shape and appearance for subcortical brain segmentation. *NeuroImage*, *56*(3), 907–922.

Pestilli, F. (2015). Test-retest measurements and digital validation for in vivo neuroscience. *Scientific Data*, *2*, 140057.

bioRxiv preprint doi: https://doi.org/10.1101/633347; this version posted May 9, 2019. The copyright holder for this preprint (which was not certified by peer review) is the author/funder, who has granted bioRxiv a license to display the preprint in perpetuity. It is made available under aCC-BY-NC-ND 4.0 International license.

Pestilli, F., Yeatman, J., Rokem, A., Kay, K., Takemura, H., & Wandell, B. (2014). LiFE: Linear Fascicle Evaluation a new technology to study visual connectomes. *Journal of Vision*, *14*(10), 1122–1122.

Petros, T. J., Rebsam, A., & Mason, C. A. (2008). Retinal axon growth at the optic chiasm: to cross or not to cross. *Annual Review of Neuroscience*, *31*, 295–315.

Prieur, D. S., & Rebsam, A. (2017). Retinal axon guidance at the midline: Chiasmatic misrouting and consequences. *Developmental Neurobiology*, *77*(7), 844–860.

Roebroeck, A., Galuske, R., Formisano, E., Chiry, O., Bratzke, H., Ronen, I., … Goebel, R. (2008). High-resolution diffusion tensor imaging and tractography of the human optic chiasm at 9.4 T. *NeuroImage*, *39*(1), 157–168.

Schmitz, B., Schaefer, T., Krick, C. M., Reith, W., Backens, M., & Käsmann-Kellner, B. (2003). Configuration of the optic chiasm in humans with albinism as revealed by magnetic resonance imaging. *Investigative Ophthalmology & Visual Science*, *44*(1), 16–21.

Smith, R. E., Tournier, J.-D., Calamante, F., & Connelly, A. (2012). Anatomically-constrained tractography: improved diffusion MRI streamlines tractography through effective use of anatomical information. *NeuroImage*, *62*(3), 1924–1938.

Smith, R. E., Tournier, J.-D., Calamante, F., & Connelly, A. (2013). SIFT: Spherical-deconvolution informed filtering of tractograms. *NeuroImage*, *67*, 298–312.

Smith, R. E., Tournier, J.-D., Calamante, F., & Connelly, A. (2015). SIFT2: Enabling dense quantitative assessment of brain white matter connectivity using streamlines tractography. *NeuroImage*, *119*, 338–351.

Smith, S. M., Jenkinson, M., Woolrich, M. W., Beckmann, C. F., Behrens, T. E. J., Johansen-Berg, H., … Matthews, P. M. (2004). Advances in functional and structural MR image analysis and implementation as FSL. *NeuroImage*, *23 Suppl 1*, S208–S219.

Staempfli, P., Rienmueller, A., Reischauer, C., Valavanis, A., Boesiger, P., & Kollias, S.

bioRxiv preprint doi: https://doi.org/10.1101/633347; this version posted May 9, 2019. The copyright holder for this preprint (which was not certified by peer review) is the author/funder, who has granted bioRxiv a license to display the preprint in perpetuity. It is made available under aCC-BY-NC-ND 4.0 International license.

(2007). Reconstruction of the human visual system based on DTI fiber tracking. *Journal of Magnetic Resonance Imaging: JMRI*, *26*(4), 886–893.

Takemura, H., Caiafa, C. F., Wandell, B. A., & Pestilli, F. (2016). Ensemble Tractography. *PLoS Computational Biology*, *12*(2), e1004692.

Tournier, J.-D., Calamante, F., & Connelly, A. (2007). Robust determination of the fibre orientation distribution in diffusion MRI: non-negativity constrained super-resolved spherical deconvolution. *NeuroImage*, *35*(4), 1459–1472.

Tournier, J.-D., Calamante, F., & Connelly, A. (2010). Improved probabilistic streamlines tractography by 2nd order integration over fibre orientation distributions. In *Proceedings of the International Society for Magnetic Resonance in Medicine* (p. 1670).

Tournier, J.-D., Calamante, F., & Connelly, A. (2013). Determination of the appropriate b value and number of gradient directions for high-angular-resolution diffusion-weighted imaging. *NMR in Biomedicine*, *26*(12), 1775–1786.

Tuch, D. S., Reese, T. G., Wiegell, M. R., Makris, N., Belliveau, J. W., & Wedeen, V. J. (2002). High angular resolution diffusion imaging reveals intravoxel white matter fiber heterogeneity. *Magnetic Resonance in Medicine: Official Journal of the Society of Magnetic Resonance in Medicine / Society of Magnetic Resonance in Medicine*, *48*(4), 577–582.

Tustison, N. J., Avants, B. B., Cook, P. A., Zheng, Y., Egan, A., Yushkevich, P. A., & Gee, J. C. (2010). N4ITK: improved N3 bias correction. *IEEE Transactions on Medical Imaging*, *29*(6), 1310–1320.

Veraart, J., Fieremans, E., & Novikov, D. S. (2016). Diffusion MRI noise mapping using random matrix theory. *Magnetic Resonance in Medicine: Official Journal of the Society of Magnetic Resonance in Medicine / Society of Magnetic Resonance in Medicine*, *76*(5), 1582–1593.

Veraart, J., Novikov, D. S., Christiaens, D., Ades-Aron, B., Sijbers, J., & Fieremans, E.

bioRxiv preprint doi: https://doi.org/10.1101/633347; this version posted May 9, 2019. The copyright holder for this preprint (which was not certified by peer review) is the author/funder, who has granted bioRxiv a license to display the preprint in perpetuity. It is made available under aCC-BY-NC-ND 4.0 International license.

(2016). Denoising of diffusion MRI using random matrix theory. *NeuroImage*, *142*, 394–406.

Wandell, B. A., Chial, S., & Backus, B. T. (2000). Visualization and measurement of the cortical surface. *Journal of Cognitive Neuroscience*, *12*(5), 739–752.

Wiegell, M. R., Larsson, H. B., & Wedeen, V. J. (2000). Fiber crossing in human brain depicted with diffusion tensor MR imaging. *Radiology*, *217*(3), 897–903.

bioRxiv preprint doi: https://doi.org/10.1101/633347; this version posted May 9, 2019. The copyright holder for this preprint (which was not certified by peer review) is the author/funder, who has granted bioRxiv a license to display the preprint in perpetuity. It is made available under aCC-BY-NC-ND 4.0 International license.

# 8. Appendices

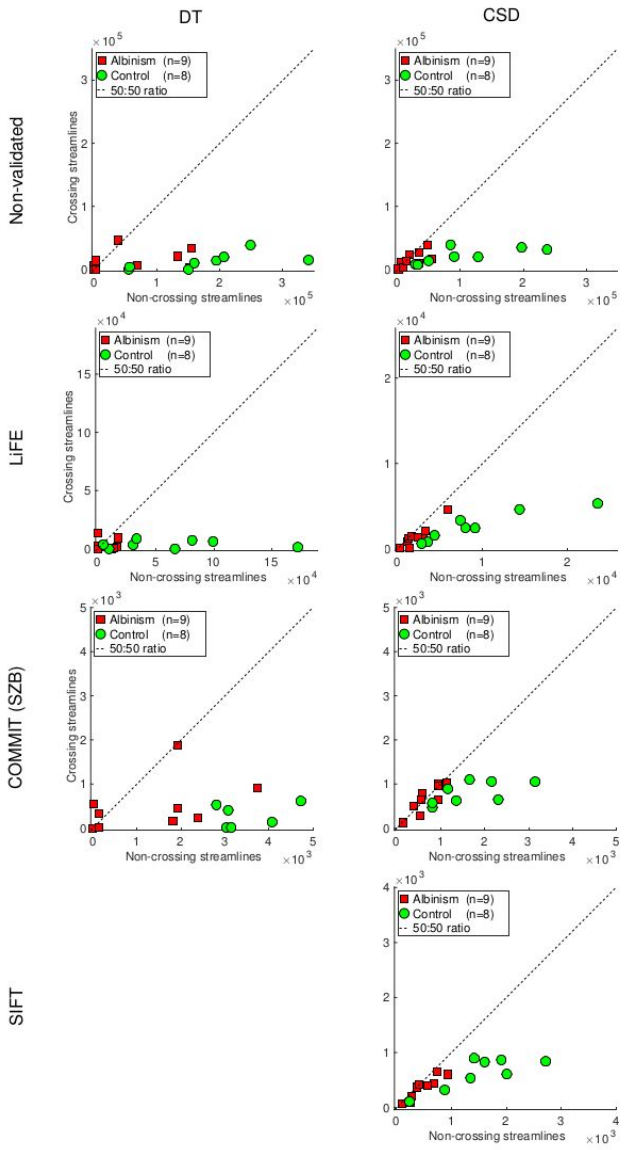


**Figure A.1. Streamline counts for all tested combinations of diffusion models and validation methods.** Numbers of crossing (x-axis) and non-crossing (y-axis) streamlines calculated from tractograms based on DT (left column) and CSD (right column) models. Rows correspond to different tested validation methods, from the top to bottom, respectively: lack of any validation, validation with LiFE, validation with COMMIT framework employing multicompartment SZB model and validation with SIFT.

bioRxiv preprint doi: https://doi.org/10.1101/633347; this version posted May 9, 2019. The copyright holder for this preprint (which was not certified by peer review) is the author/funder, who has granted bioRxiv a license to display the preprint in perpetuity. It is made available under aCC-BY-NC-ND 4.0 International license.

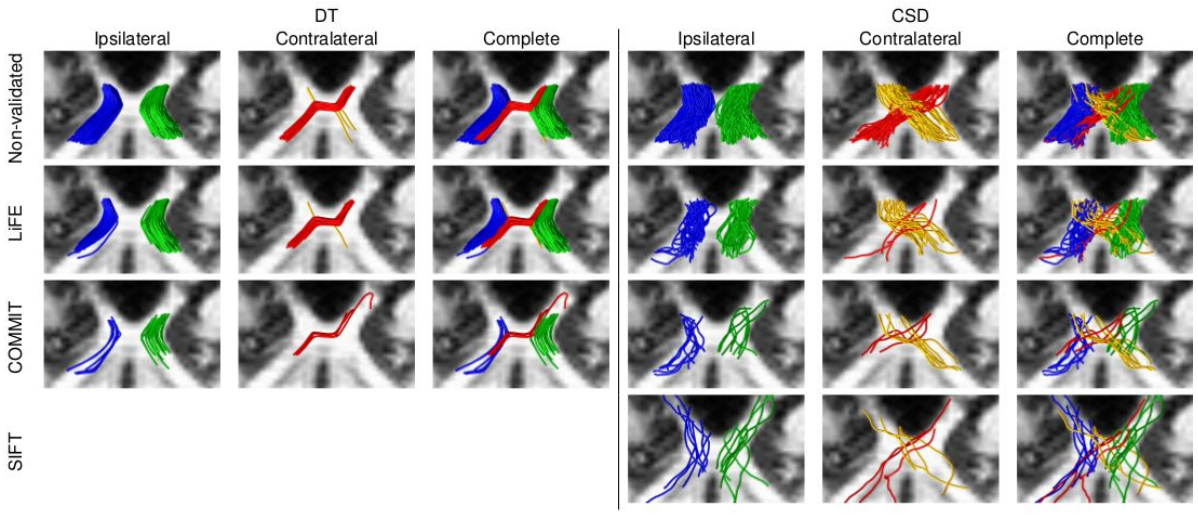


**Figure B.1. Qualitative tracking results for exemplary control subject.** Exemplary subsets (1% of a total number of streamlines) of tractograms for DT- (left column) and CSD-based (right column) based modelling. Streamlines traversing optic chiasm ipsilaterally (left sub-columns) and streamlines crossing optic chiasm to contralateral brain hemisphere (middle sub-columns) were merged into single group of streamlines (right sub-columns). Rows correspond to different tested validation methods, from the top to bottom, respectively: lack of any validation, validation with LiFE, validation with COMMIT framework employing multicompartment SZB model and validation with SIFT.

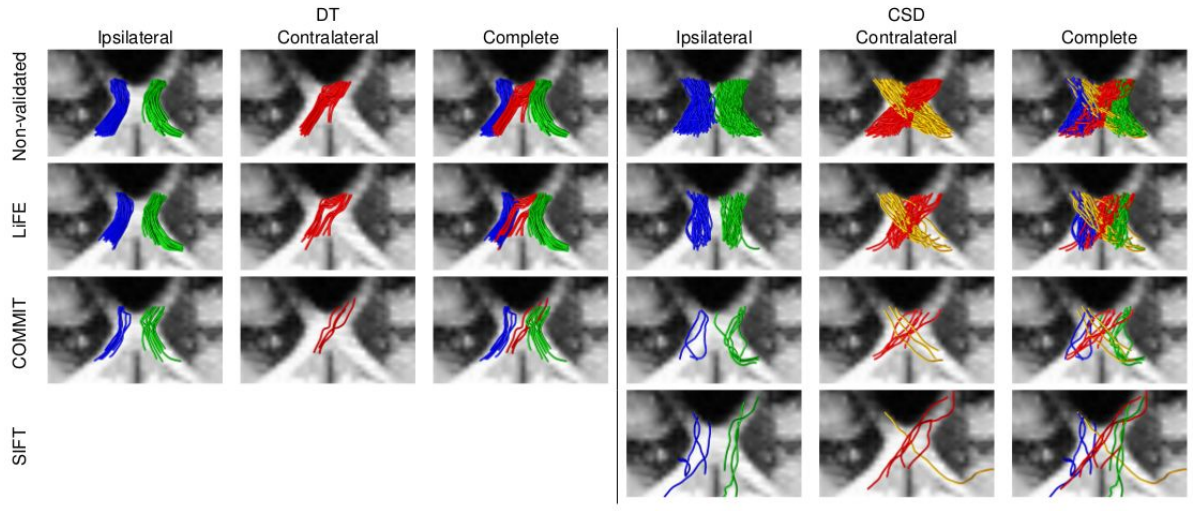


**Figure B.2. Qualitative tracking results for exemplary participant with albinism.** Conventions as in **Figure B.1**.